

Node-line Dirac semimetal manipulated by Kondo mechanism in nonsymmorphic CePt₂Si₂

Hao-Tian Ma,¹ Xing Ming,¹ Xiao-Jun Zheng,¹ Jian-Feng Wen,¹ Yue-Chao Wang,² Yu Liu,² and Huan Li^{1,*}

¹College of Science, Guilin University of Technology, Guilin 541004, China

²Laboratory of Computational Physics, Institute of Applied Physics and Computational Mathematics, Beijing 100088, China

(Dated: December 7, 2022)

Dirac node lines (DNLs) are characterized by Dirac-type linear crossings between valence and conduction bands along one-dimensional node lines in the Brillouin zone (BZ). Spin-orbit coupling (SOC) usually shifts the degeneracy at the crossings thus destroys DNLs, and so far the reported DNLs in a few materials are non-interacting type, making the search for robust interacting DNLs in real materials appealing. Here, via first-principle calculations, we reveal that Kondo interaction together with nonsymmorphic lattice symmetries can drive a robust interacting DNLs in a Kondo semimetal CePt₂Si₂, and the feature of DNLs can be significantly manipulated by Kondo behavior in different temperature regions. Based on the density function theory combining dynamical mean-field theory (DFT+DMFT), we predict a transition to Kondo-coherent state at coherent temperature $T_{\text{coh}} \approx 80$ K upon cooling, verified by temperature dependence of Ce-4*f* self-energy, Kondo resonance peak, magnetic susceptibility and momentum-resolved spectral. Below T_{coh} , well-resolved narrow heavy-fermion bands emerge near the Fermi level, constructing clearly visualized interacting DNLs locating at the BZ boundary, in which the Dirac fermions have strongly enhanced effective mass and reduced velocity. In contrast, above a crossover temperature $T_{\text{KS}} \approx 600$ K, the destruction of local Kondo screening drives non-interacting DNLs which are comprised by light conduction electrons at the same location. These DNLs are protected by lattice nonsymmorphic symmetries thus robust under intrinsic strong SOC. Our proposal of DNLs which can be significantly manipulated according to Kondo behavior provides a unique realization of interacting Dirac semimetals in real strongly correlated materials, and serves as a convenient platform to investigate the effect of electronic correlations on topological materials.

I. INTRODUCTION

Dirac semimetals, such as Na₃Bi¹ and Cd₃As₂², are characterized by linear crossings between valence and conduction bands in momentum space, forming four-fold-degenerate Dirac points describing by Dirac equation, and can be viewed as three-dimensional (3D) analogy of the two-dimensional (2D) Dirac points in graphene. Under breaking of either time-reversal or space-inversion symmetry, individual Dirac point can be divided into a pair of Weyl points with opposite chiralities, as observed in TaAs³ and Ag₂S⁴, etc. In some materials with negligible spin-orbital coupling (SOC), the valence and conduction bands meet along a curved line or closed loop in the Brillouin zone, forming Dirac node lines (DNLs), which are usually unstable under action of SOC. Recently, DNLs in materials with space groups No. 129 and 125 are proposed and confirmed by angle-resolved photoemission spectrums (ARPES) observations. In these materials such as ZrSiS⁵⁻⁷ and PtPb₄⁸, the DNLs are protected by nonsymmorphic symmetries in their lattice space group, making them robust under SOC. Additionally, the Dirac fermions on these DNLs exhibit 2D character in momentum space⁹.

In contrast to ZrSiS and PtPb₄, in which the electronic correlations are negligible, strong correlations may bring dramatic affects to the DNLs. As in the case of Weyl-Kondo semimetal Ce₃Bi₄Pt₃^{10,11}, the strong correlation and Kondo hybridization result in renormalized Weyl fermions with highly enhanced effective mass and suppressed Fermi velocity, leading to characteristic T^3 dependence of specific heat¹⁰, more remarkably, the correlations can give rise to non-linear response behaviors such as giant spontaneous Hall effect^{12,13}. Similarly, the electron correlations in material with DNLs may also induce notable affects to the Dirac fermions

and arouse anomalous transport phenomena which can be explored in future experiments, nevertheless, such interacting DNLs seem lack of report in the literature yet.

In this article, we systematically explore nonsymmorphic Kondo semimetals CePt₂Si₂ and CePt₂Ge₂ by density-function theory combing with dynamical mean-field theory (DFT+DMFT). Firstly, we find that below a characteristic Kondo coherence temperature at about 80 K, CePt₂Si₂ becomes Kondo-coherent, forming interacting DNLs by heavy quasi-particles composed of conduction *spd* electrons and Ce-4*f* electrons. Secondly, above another crossover temperature at about 600 K, the local Kondo screening in CePt₂Si₂ has been destructed, hence the DNLs become non-interacting, consisting of only light conduction electrons. Due to larger unit cell volume, the DNLs in CePt₂Ge₂ remains non-interacting in all calculated temperature region. DNLs are also reported in a few rare-earth compounds such as centrosymmetric CeRhSb and CeNiSn¹⁴, however, the correlated 4*f* electrons in those materials are already localized thus their DNLs are actually created by conduction electrons only. In this context, to the best of our knowledge, CePt₂Si₂ provides the first studied material with interacting DNLs in real strongly correlated materials.

The rest of this paper is arranged as follows. In section 2, we will analyse the crystal structures of CePt₂Si₂ and CePt₂Ge₂, and introduce the technical details of DFT+DMFT simulations in present work. In section 3, we will present the DFT+DMFT results of CePt₂Si₂. Through synthetically analysis of self-energy, density of state, momentum-resolved spectral and the magnetic susceptibility, we will evaluate the two characteristic temperature, firstly the Kondo coherent temperature driving the formation of coherent heavy-fermion hybridization bands, secondly the Kondo screening tempera-

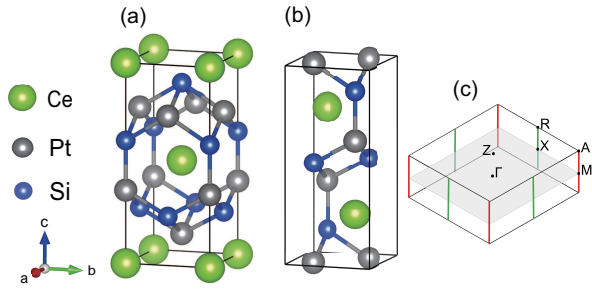


FIG. 1: (a) Primitive unit cell of CePt_2Si_2 with tetragonal CaBa_2Ge_2 type structure. (b) Equivalent unit cell displaying inversion and nonsymmorphic symmetries. (c) Corresponding Brillouin zone, in which the red and green lines denotes the DNLs along M-A and X-R paths, respectively.

ture below which the local Kondo screening of $4f$ electrons by conduction electrons turns on. In sections 4, we will discuss the emergence of interacting DNLs in CePt_2Si_2 below Kondo-coherent temperature, and also the non-interacting DNLs above the Kondo screening temperature. We will also verify the non-interacting DNLs in CePt_2Ge_2 based on its DFT and DFT+DMFT results. The last section will give a brief conclusion and discussion.

II. CRYSTAL STRUCTURE AND COMPUTATIONAL METHOD

The primitive unit cell of CePt_2Si_2 is illustrated in Fig. 1(a), which crystallizes in the tetragonal CaBa_2Ge_2 type structure with space group $P4/nmm$ (No. 129). The lattice constants and atom positions of CePt_2Si_2 and isostructural CePt_2Ge_2 are collected in Tab. I according to Ref. 15. From an alternate set of unit cell of CePt_2Si_2 in Fig. 1(b), the space inversion symmetry can be clearly seen. Besides the inversion symmetry, CePt_2Si_2 and CePt_2Ge_2 exhibit nonsymmorphic symmetries combining point group and fractional translation operations, namely the gliding mirror plane $\{M_z|\frac{1}{2}, \frac{1}{2}\}$ and screw axes $\{C_{2x}|\frac{1}{2}, 0\}$, $\{C_{2y}|0, \frac{1}{2}\}$, where the origin of axes locate at the center of the unit cell in Fig. 1(b). CePt_2Si_2 was found to remain paramagnetic as low as 0.06 K¹⁶, signaling the preservation of time-reversal symmetry. The nonsymmorphic symmetries combining time-reversal and inversion symmetries protect the four-fold degeneracy at X and M, and also along X-R and M-A lines in the Brillouin zone, creating the DNLs shown in Fig. 1(c), as will be discussed in detail below.

In order to explore the electron-correlation effects in CePt_2Si_2 and CePt_2Ge_2 , we employ the density function theory combined with single-site dynamical mean-field theory (DFT+DMFT) embodied in the EDMFT package¹⁷, with the DFT part implemented by full-potential linear augmented plane-wave method built in WIEN2k code¹⁸. Such DFT+DMFT method has been successfully applied in studying electronic correlations in a variety of materials, especially in rear-earth compounds^{14,19-23}. In the DFT part, we use a

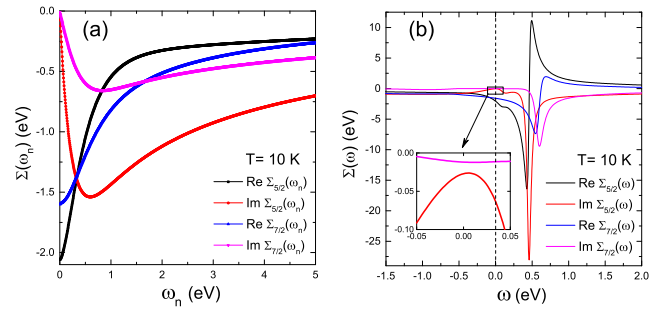


FIG. 2: Self-energies of $4f_{5/2}$ and $4f_{7/2}$ states via DFT+DMFT calculations of CePt_2Si_2 at 10 K on (a) imaginary-frequency axis and (b) real-frequency axis. Inset of (b) shows the detail near zero frequency.

$16 \times 16 \times 7$ k-mesh in the Brillouin zone integration, with a cut-off parameter K_{max} given by $R_{\text{MT}}K_{\text{max}} = 7.0$, and spin-orbital coupling (SOC) is included throughout the calculations. The DFT band structures are also cross-checked by VASP code. Each DFT+DMFT step contains one-shot DMFT and 20 steps of DFT calculations. In the DMFT iterations, in order to better fit experiment observations, we employ the on-site Coulomb repulsion $U = 5.0$ eV and Hund's coupling $J_H = 0.76$ eV on Ce-4f orbits, similar to the value set in Refs. 20 and 14. The states within energy window $[-10$ eV, 10 eV] from the Fermi level are projected into the Anderson impurity problems. We use the continuous-time quantum Monte Carlo method (CT-QMC) to solve the Anderson impurity problems, then perform analytical continuation by maximum-entropy method to obtain the real-frequency self-energies for f electrons. In each CT-QMC computation, 128 CPU cores are used to run $(5 \sim 30) \times 10^8$ QMC steps from 1000 K to 10 K. Typically, within 30~40 DFT+DMFT iterations, full-charge self consistency can be reached, then we run additional 5 iterations to further average the self-energies. Since no magnetic order was found in CePt_2Si_2 and CePt_2Ge_2 down to 60 mK¹⁶, we focus on the paramagnetic phase. In the impurity solver, the crystal-field splitting of f orbitals has been examined and is found to be one more orders of magnitude smaller than the SOC splitting, hence the crystal-field splitting is neglected in present calculations. The SOC splits Ce-4f orbitals into $j = 5/2$ and $j = 7/2$ states, denoted by $4f_{5/2}$ and $4f_{7/2}$ respectively in the following.

III. CORRELATION EFFECT AND KONDO BEHAVIOR

In DFT+DMFT formulations, the electron correlation manifests itself following the local self-energies of f states. In Fig. 2, we plot the calculated DFT+DMFT local self-energies $\Sigma(\omega_n)$ and $\Sigma(\omega)$ for CePt_2Si_2 at temperature $T=10$ K, on imaginary- and real-frequency axes respectively, where Matsubara frequency $\omega_n = (2n + 1)\pi T$. In Fig. 2 (a), the imaginary-part self-energies for both $4f_{5/2}$ and $4f_{7/2}$ states nicely approach zero at zero imaginary frequency, indicating Fermi-liquid like character. The slope of imaginary-part self-

TABLE I: Crystal parameters of CePt₂Si₂ and CePt₂Ge₂¹⁵, the atomic positions correspond to Fig.1(b).

	lattice parameters	Ce position	Pt position	Si position
CePt ₂ Si ₂	a=b=4.252Å c=9.788Å	Ce(2c):($\frac{1}{4}, \frac{1}{4}, 0.7452$), ($\frac{3}{4}, \frac{3}{4}, 0.2548$)	Pt(2c):($\frac{1}{4}, \frac{1}{4}, 0.3798$), ($\frac{3}{4}, \frac{3}{4}, 0.6202$)	Si(2c):($\frac{1}{4}, \frac{1}{4}, 0.1329$), ($\frac{3}{4}, \frac{3}{4}, 0.8671$)
CePt ₂ Ge ₂	a=b=4.397Å c=9.802Å	Ce(2c):($\frac{1}{4}, \frac{1}{4}, 0.74$), ($\frac{3}{4}, \frac{3}{4}, 0.26$)	Pt(2c):($\frac{1}{4}, \frac{1}{4}, 0.383$), ($\frac{3}{4}, \frac{3}{4}, 0.617$)	Ge(2c):($\frac{1}{4}, \frac{1}{4}, 0.131$), ($\frac{3}{4}, \frac{3}{4}, 0.869$)
			Pt(2a):($\frac{1}{4}, \frac{3}{4}, 0$), ($\frac{3}{4}, \frac{1}{4}, 0$)	Si(2b):($\frac{1}{4}, \frac{3}{4}, \frac{1}{4}$), ($\frac{3}{4}, \frac{1}{4}, \frac{1}{2}$)
			Pt(2a):($\frac{1}{4}, \frac{3}{4}, 0$), ($\frac{3}{4}, \frac{1}{4}, 0$)	Ge(2b):($\frac{1}{4}, \frac{3}{4}, \frac{1}{4}$), ($\frac{3}{4}, \frac{1}{4}, \frac{1}{2}$)

energy $\text{Im}\Sigma_{5/2}(\omega_n)$ for $4f_{5/2}$ state at zero frequency is about -9.3, which gives the quasi-particle spectral weight and mass enhancement factor

$$Z = 1 / (1 - \frac{\partial \Sigma(\omega_n)}{\partial \omega_n} |_{\omega_n \rightarrow 0^+}) = 0.097, \quad (1)$$

$$m^* / m_{DFT} = 1 / Z = 10.3,$$

respectively, it means that the band width of $4f_{5/2}$ bands are strongly reduced to be roughly ten times narrow than in DFT, as will be verified in the following. Large value of m^* / m_{DFT} is the origin of large specific heat of CePt₂Si₂ observed at low temperature²⁴. The self-energies on real axis are created through analytical continuation of $\Sigma(\omega_n)$ by maximum entropy method, and are shown in Fig.2 (b). The real-part self-energies for both $4f_{5/2}$ and $4f_{t/2}$ states show rapid variations between $\omega=(0.2 \text{ eV}, 1 \text{ eV})$, leading to significant modifies of f bands from DFT results by correlations, as will be seen below. At $T=10 \text{ K}$, the imaginary self-energy $\text{Im}\Sigma_{5/2}(\omega)$ of $4f_{5/2}$ state has a small value 27.2 meV at $\omega = 0$, gives rise to low scattering rate and relatively long lift time for quasi particles at the Fermi level.

Fig.3(a) demonstrates the evolution of imaginary self-energy $\text{Im}\Sigma_{5/2}(\omega)$ for $4f_{5/2}$ state as a function of frequency ω , at various temperatures. Below 80 K, a clear and sharp dip near $\omega = 0$ appears, reaching a quite small value at the bottom. Such dip of $\text{Im}\Sigma_{5/2}(\omega)$ near $\omega = 0$ directly drives an intense Kondo resonance peak in the $4f_{5/2}$ density of states (DOS) (see below), and can be interpreted as the onset of Kondo coherence^{20,21} below a characteristic coherent temperature $T_{\text{coh}} \approx 80 \text{ K}$. Moreover, the sharp dip of $\text{Im}\Sigma_{5/2}(\omega)$ below T_{coh} also induces clearly resolved $4f$ bands, further verifying the Kondo coherence below T_{coh} , as will be discussed below. Besides, below 80 K, $\text{Im}\Sigma_{5/2}(\omega)$ can be well fitted by a parabolic function $\text{Im}\Sigma_{5/2}(\omega) \approx -\alpha(\omega - \omega_0)^2 - \Sigma_0$, with $\alpha = 29.7 \text{ eV}^{-1}$, $\omega_0 = 5 \text{ meV}$, $\Sigma_0 = 26.5 \text{ meV}$ at 10 K, also suggesting Fermi-liquid behavior at low temperature, in accordance with the interpretation from resistivity and specific heat experiments^{24,25}. As temperature rises, the dip of $\text{Im}\Sigma_{5/2}(\omega)$ is suppressed gradually, while above 600 K, the narrow dip seem to vanish, leaving a broad minimum considerably away from $\omega = 0$, resulting in a greatly weakened $4f$ DOS. In Fig.3(b), the magnitude of $-\text{Im}\Sigma_{5/2}(\omega = 0)$ is plotted as temperature varies. Below 10 K, $-\text{Im}\Sigma_{5/2}(0)$ tends to be saturated and approaches about 27 meV at zero temperature, while temperature rises, it shows a gradually increase, then turns to stay around large magnitude of 1.25 eV at $T > 600 \text{ K}$, which makes $4f$ electrons localized at high temperature, as will be further clarified below.

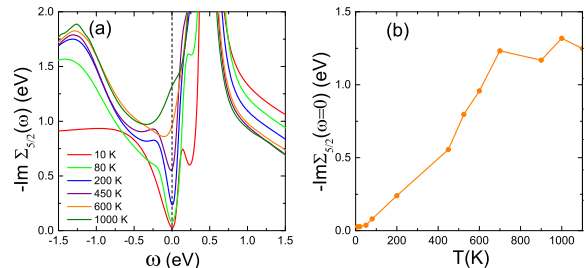


FIG. 3: (a) Imaginary part of $4f_{5/2}$ self-energy $\text{Im}\Sigma_{5/2}(\omega)$ vs ω at different temperatures. (b) Evolution of $\text{Im}\Sigma_{5/2}(\omega = 0)$ with temperature.

The many-body Kondo screening of local $4f$ electrons by conduction electrons creates an enormous enhancement in the DOS of Ce- $4f$ states near the Fermi level, i.e., the Kondo resonance peak. In order to further clarify the onset of Kondo coherence and Kondo screening, we calculate the DOS of CePt₂Si₂ with varying temperature. In Fig.4 (a), the total and $4f$ DOS are plotted as functions of energy, from 10 K to 1000K, displaying significant difference near the Fermi level as temperature rises. At low temperatures (see 10 K and 80 K cases), two narrow peaks (peak width about 20 meV) dominated by $4f$ states appear with large height, in which the one contributed by $4f_{5/2}$ state centers at 14 meV above the Fermi level with its tail crosses E_F , the other owing to $4f_{7/2}$ state locates at 0.351 eV above E_F , and the corresponding SOC splitting between these two peaks is about 0.337 eV, as shown in Fig.4 (b). As temperature increases, the two resonance peaks decrease considerably but are still visible up to 1000 K. The robust of $4f$ DOS peaks at high temperature is owing to relatively strong impurity hybridization function in DMFT calculation, which indicates a strong c - f hybridization in CePt₂Si₂ in wide temperature range. Since the Kondo resonance peak is dominated by the low-lying $4f_{5/2}$ state, we plot the evolution of its peak height vs temperature in Fig.4 (c). It can be seen that the Kondo resonance peak carries large height at low temperatures and shows a saturation tendency below 10 K, which arises from similar saturation behavior of $-\text{Im}\Sigma_{5/2}(0)$ in Fig.3. As temperature rises from 10 K, the peak height first drops rapidly, then turns to decrease much slowly, and eventually varies smoothly to maintain a small magnitude above 600 K. Around 80 K, the Kondo coherence sets in and manifests itself by a rapid increase of resonance peak, further confirming the appearance of Kondo coherence below coherent temperature $T_{\text{coh}} \approx 80 \text{ K}$. While above 600 K, Kondo resonance peak is greatly reduced, and only accounts

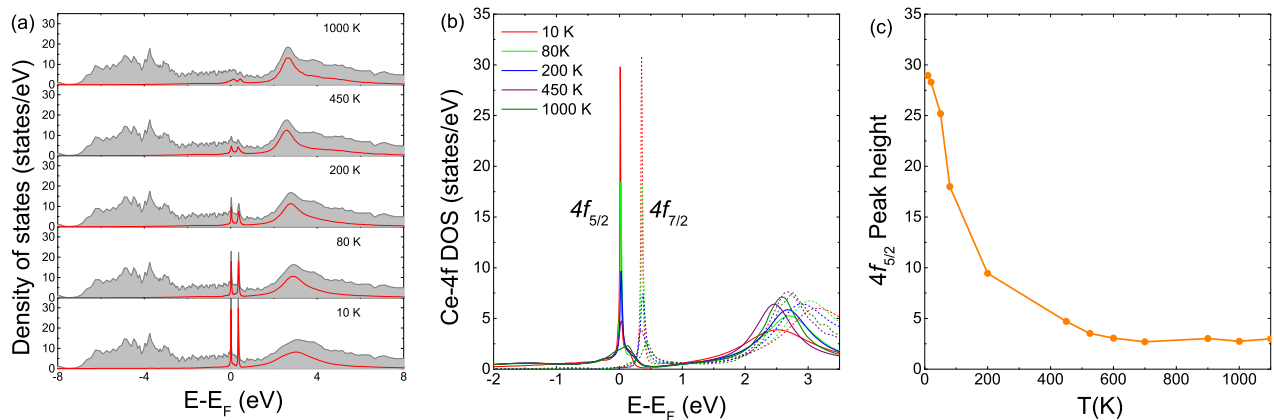


FIG. 4: (a) Density of states (DOS) of CePt_2Si_2 from temperature 10 K to 1000 K via DFT+DMFT calculations. The grey solid lines denote total DOS, and the red lines denote Ce-4*f* DOS. The paired 4*f* peaks become more and more prominent as temperature drops. (b) Projected Ce-4*f* DOS at different temperatures. The solid lines denote $4f_{5/2}$ DOS, while the dashed lines denote $4f_{7/2}$ DOS. The splitting of 4*f* DOS is caused by SOC. (c) Temperature variation of $4f_{5/2}$ peak height, implying formation of local Kondo screening and Kondo resonance below $T_{\text{KS}} \approx 600$ K.

for a small proportion in the total DOS, indicating that the 4*f* electrons are already localized to form local moments, similar to the 4*f* states in CeSb, CeIrIn₅ and CeIn₃ in their corresponding local-moment parameter regions^{19,20,26}. Therefore, we obtain another characteristic temperature $T_{\text{KS}} \approx 600$ K, below which the conduction *spd* electrons start to screen the localized Ce-4*f* electrons to form Kondo singlet states, and consequently generate Kondo resonance peak gradually in 4*f* DOS near the Fermi level. Apart from the resonance peaks, the on-site Coulomb repulsion between 4*f* electrons also produces broad lower and upper Hubbard bands in the 4*f* DOS, concentrated mainly between (-3, -1) eV and (1.5, 4) eV from the Fermi level respectively, and the distance between their centers is roughly 4.3 eV, comparable with Hubbard strength $U=5$ eV. Besides, there is very little DOS weight in the lower Hubbard band thus hard to identify, while the upper Hubbard band has large intensity in the DOS.

We now turn to the magnetic susceptibility of CePt_2Si_2 . In Fig.5, the local spin susceptibility χ_s and its inverse χ_s^{-1} are illustrated as functions of temperature, computed during the CT-QMC loop in DMFT iterations. In Fig.5(a), χ_s shows a faster increase upon cooling, then undergoes an abrupt decrease below 80 K. At $T > 80$ K, χ_s can be well fitted by the Curie-Weiss form $\chi_s = C/(T + \theta)$ with $\theta \approx 92$ K, and starts to deviate from the Curie-Weiss formula considerably below 80 K. Such temperature dependence of magnetic susceptibility shows consistency with experimental results^{24,25,27}, and provides strong evidence of the appearance of Kondo coherence below coherence temperature $T_{\text{coh}} = 80$ K, similar to Kondo semimetal $\text{CeFe}_2\text{Al}_{10}$ ²⁸.

The above analyses of 4*f* self-energies, Kondo resonance peak and magnetic susceptibility clearly witness a Kondo mechanism of CePt_2Si_2 . Above a crossover temperature $T_{\text{KS}} \approx 600$ K, the Ce-4*f* electrons are tightly bound and fully localized inside Ce atoms, thus are totally decoupled from itinerant electrons to form local moments. Reduction of tem-

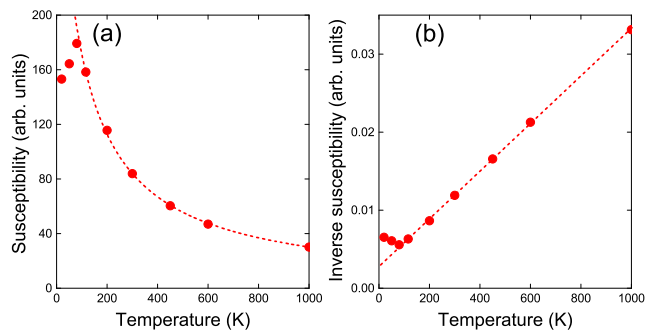


FIG. 5: Red dots show the temperature dependence of (a) local magnetic susceptibility χ_s and (b) inverse susceptibility χ_s^{-1} for CePt_2Si_2 , via DMFT calculations. For comparison, the Curie-Weiss form $\chi_s = C/(T + \theta)$ is denoted by red dashed lines.

perature from T_{KS} induces local Kondo screening of local moments by conduction electrons gradually, results in Kondo singlet states and arouses Kondo resonance peak near the Fermi level. Further cooling to below $T_{\text{coh}} \approx 80$ K drives additional indirect non-local Ruderman-Kittel-Kasuya-Yosida (RKKY) interaction between *f* electrons²⁹, which creates a Kondo-coherent many-body state and gives rise to intense Kondo resonance peak and well resolved heavy-fermion hybridization bands.

IV. THE DIRAC NODE LINES

The transition to Kondo coherent state below T_{coh} can be witnessed by temperature variation of spectral function, which can be measured directly via ARPES experiments. In Fig.6, the momentum-resolved spectral function $A(\mathbf{k}, \omega)$ of CePt_2Si_2 calculated by DFT+DMFT is plotted along a repre-

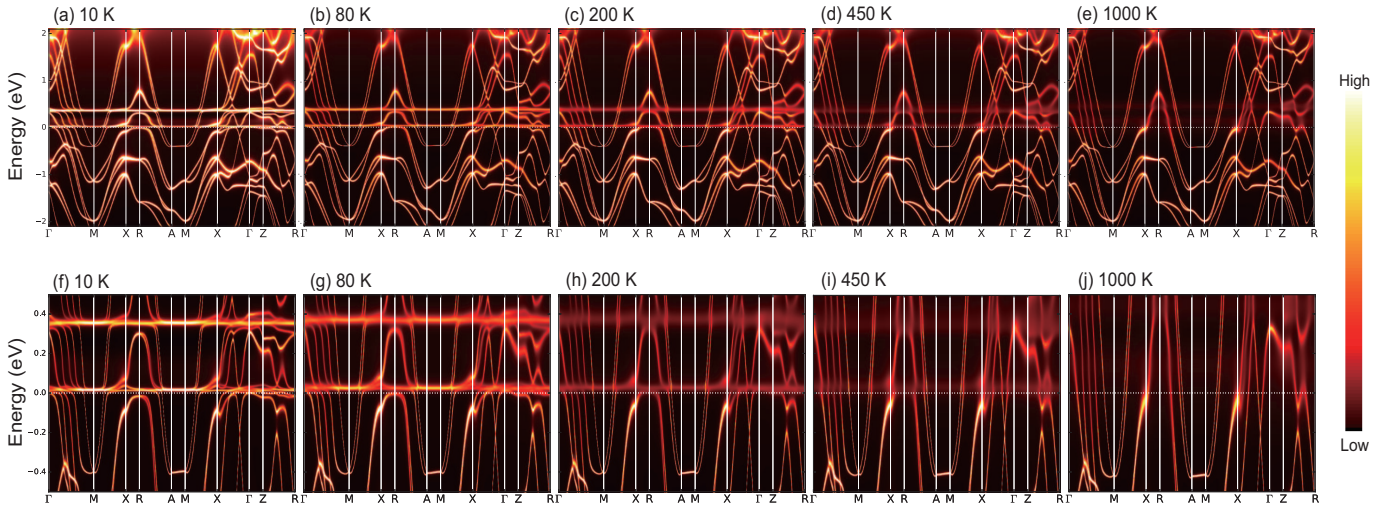


FIG. 6: DFT+DMFT momentum-resolved spectral function of CePt_2Si_2 from 10 K to 1000 K. The bottom patterns are just zoomed-in view of top patterns. From 10 K to 80 K, the hybridization bands near the Fermi level are clearly resolved, while at 1000 K, the hybridization bands are already blurred out (in (e) and (i)), leaving highly-dispersive conduction bands and signaling local-moment nature of Ce-4*f* electrons at high temperature.

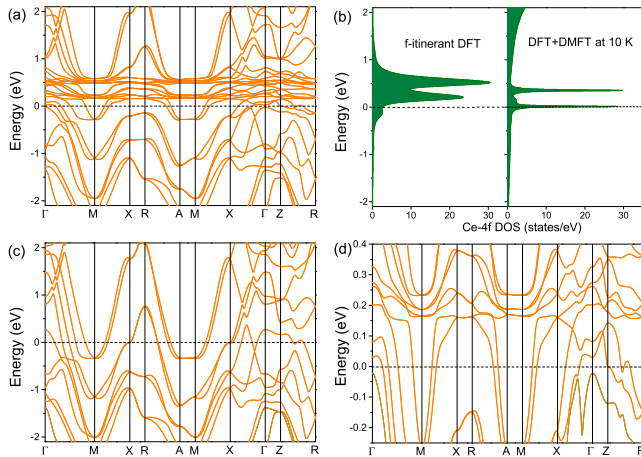


FIG. 7: DFT bands of CePt_2Si_2 treating Ce-4*f* electrons as (a) itinerant and (c) open-core. (d) is just a zoomed-in view of (a) near the Fermi level. The bands are degenerate at X, R, M, A and along X-R and M-A paths, leading to DNLs locating on X-R and M-A lines shown in Fig.1(c). Ce-4*f* bands in (a) has been divided into $4f_{5/2}$ and $4f_{7/2}$ bands under SOC splitting, contributing double 4*f* DOS peaks in (b), by comparison, DFT+DMFT calculation leads to much narrow 4*f* DOS peaks at 10 K.

sentative high-symmetry path in the Brillouin zone, in temperature range from 10 K to 1000 K. At low temperatures (10 K and 80 K cases), the intense spectral weight of two groups of weakly dispersive heavy-fermion bands, which concentrate near 14 meV and 0.351 eV above the Fermi level, respectively, can be clearly seen, through which the two narrow resonance peaks in DOS (Fig.4(a)) can be directly obtained

via momentum integral of spectral function through $\rho(\omega) = \sum_{\mathbf{k}} A(\mathbf{k}, \omega)$. These two groups of hybridization bands are constructed through *c-f* hybridization between conduction *spd* electrons with Ce- $4f_{5/2}$ or $4f_{7/2}$ states, respectively, resulting in heavy-fermion quasi-particles with enhanced effective mass m^* determined by Eq.1. The sharply resolved heavy-fermion bands near the Fermi level below 80 K again verifies formation of Kondo coherence below $T_{\text{coh}} \approx 80$ K. As temperature rises from T_{coh} , the hybridization bands become more and more blurred and are no longer well resolved.

Above the local Kondo screening temperature $T_{\text{KS}} \approx 600$ K, the intensity of hybridization bands is dramatically diminished (see Fig.6(e) at 1000K), leading to small magnitude of 4*f* DOS peaks (see the top pattern in Fig.4(a)), consequently the 4*f* electrons are fully localized, and the bands near the Fermi level become highly dispersive, see Fig.6(j). Fig.7(c) shows the DFT bands treating 4*f* orbitals as open-core states³⁰, which can nicely reproduce high-temperature DFT+DMFT result in Fig.6(e), further confirming the local-moment nature of 4*f* states at $T > T_{\text{KS}}$. It should be noted that the spectral weight of 4*f* electrons remains non-vanished even at $T > T_{\text{KS}}$, similar to γ -Ce, CeSb and CeIn₃ in their local-moment regions^{19,21,26}.

At 10 K, the DFT+DMFT hybridization bands around 14 meV above the Fermi level are clearly distinguishable, see Fig.6(f) and enlarged view in Fig.8(a), in which the band structure is indeed similar to that of the DFT bands in Fig.7(a) and (d) which treat Ce-4*f* electrons to be itinerant. The hybridization bands of *f*-itinerant DFT also split into $4f_{5/2}$ and $4f_{7/2}$ bands by an energy interval 0.31 eV, close to the SOC splitting by 0.337 eV in DFT+DMFT simulation. As shown in Fig.7(b), the 4*f* DOS shows three major differences between DFT and DFT+DMFT results, firstly, the 4*f* peak width (198 meV in DFT) is strongly reduced to 20 meV in DFT+DMFT under electron correlations, with a reduction factor of 9.9

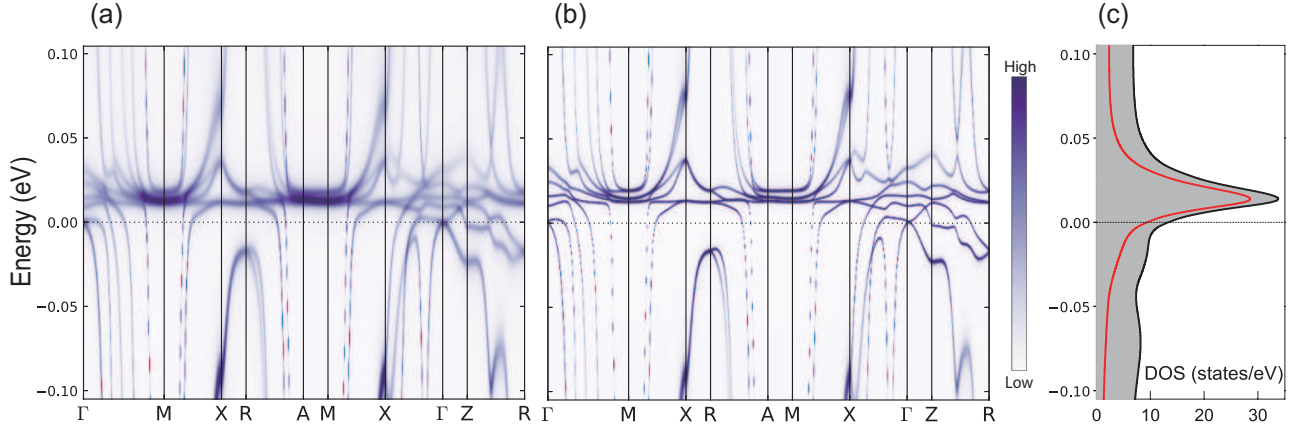


FIG. 8: (a) DFT+DMFT momentum-resolved spectral function of CePt_2Si_2 near Fermi energy at 10 K. (b) Modify $\text{Im}\Sigma_{5/2}(\omega)$ to see the low-lying hybridization bands and their crossings more clearly. (c) DFT+DMFT DOS at 10 K, in which the black line denotes total DOS, red line shows DOS of $4f_{5/2}$ state.

close to the mass enhancement $m^*/m_{\text{DFT}} = 1/Z = 10.3$; secondly, in DFT+DMFT result, the $4f_{5/2}$ DOS shifts towards the Fermi level, forming Kondo resonance peak very close to the Fermi energy, while the DFT $4f_{5/2}$ DOS peak locates considerable higher above the Fermi level; thirdly, DFT+DMFT produces additional lower and upper Hubbard bands far away from the Fermi level.

In the literature, it has been shown that the nonsymmorphic symmetries combining point group and fractional translation operations can generate additional degeneracy along certain high-symmetry paths in the Brillouin zone, which are robust under action of SOC⁹. In space group No. 129, the nonsymmorphic symmetries are the gliding mirror plane $\{M_z|\frac{1}{2}, \frac{1}{2}\}$ and screw axes $\{C_{2x}|\frac{1}{2}, 0\}$, $\{C_{2y}|0, \frac{1}{2}\}$, which are hold by CePt_2Si_2 and CePt_2Ge_2 crystals in Fig.1(b). At $T > T_{\text{KS}}$, since Ce- $4f$ electrons are already localized, the electron bands of CePt_2Si_2 can be reflected by $4f$ open-core DFT results in Fig.7(c). With time-reversal symmetry in their paramagnetic phases, the space inversion symmetry of CePt_2Si_2 and CePt_2Ge_2 guarantees global two-fold degeneracy of the electron bands, and the nonsymmorphic symmetries give additional degeneracy of bands at X, R, M, A points, therefore, four-fold Dirac crossings arise, generating Dirac nodes at these points. Moreover, degeneracy of bands remain along X-R and M-A paths (see Fig.7(c)), resulting in DNLs, similar to ZrSiS and PtPb_4 ⁵⁻⁸. The X-R and M-A DNLs locate at the boundary of the Brillouin zone, as shown in Fig.1(c). The energy ranges of the X-R DNLs in CePt_2Si_2 are (-0.725 eV, -0.624 eV) and (6.4 meV, 0.759 eV) from the Fermi level, while for M-A DNLs it is in (-0.338 eV, -0.330 eV). At $T > T_{\text{KS}}$, the similarity between spectral function (Fig.6(e)) and $4f$ open-core bands in Fig.7(c) clearly verifies above analysis of band-crossings and appearance of DNLs in CePt_2Si_2 in local-moment region. It should be stressed that since the Ce- $4f$ electrons are already localized at $T > T_{\text{KS}}$, such DNLs are non-interacting and are composed by light conduction electrons (mostly Ce- d , Pt- p,d , and Si- p electrons).

We have shown in Fig.6(f) and Fig.8(a) that below $T_{\text{coh}} \approx$

80 K, the hybridization bands can be clearly identified near the Fermi level, in which their crossings at X, R and along X-R path are already legible, while at M, A and along M-A path seem a little fuzzy because several crossings concentrate in a narrow energy range. In order to see the DNLs more clearly, we slightly reduce the value of Σ_0 in the parabolic expression of imaginary self-energy $\text{Im}\Sigma_{5/2}(\omega)$ and recalculate the spectral. The obtained spectral function is displayed in Fig.8(b), in which the locations of crossings between hybridization bands match f -itinerant DFT results in Fig.7(d), confirming the existence of interacting DNLs along X-R and M-A paths, since such crossings are protected by lattice nonsymmorphic symmetries and robust under electron correlations. Nevertheless, below T_{coh} , electron correlations push the hybridization bands much closer to the Fermi level than f -itinerant DFT results, hence generate much narrow energy windows for X-R and M-A DNLs, which are about (-90 meV, -15 meV) and (12.5 meV, 37 meV) along X-R, and (12.5 meV, 18.8 meV) along M-A, from the Fermi level. Compare Fig.8(a) and (c), it can be seen that the energy window of M-A DNLs locates at the center of the Kondo resonance peak, therefore, the Dirac fermions near M-A DNLs are highly renormalized and are essentially the heavy-fermions hybridizing $4f_{5/2}$ electrons with conduction electrons. The energy window of X-R DNLs locates at the lower tail of the Kondo resonance peak, thus the Dirac fermions near X-R DNLs are also interacting.

From above discussions, we can now verify the appearance of interacting DNLs in CePt_2Si_2 , locating along X-R and M-A paths in its Brillouin zone, driven by Kondo coherence below coherent temperature $T_{\text{coh}} \approx 80$ K, and the energy windows of these DNLs are very close to the Fermi level. The Dirac fermions of these interacting DNLs are constructed by heavy-fermions with strongly enhanced effective mass and reduced velocity. As temperature rises from T_{coh} , the interacting DNLs are destructed gradually and are no longer clearly identified. Above the local Kondo screening temperature $T_{\text{KS}} \approx 600$ K, the DNLs reappear near the Fermi level, but now the correlated $4f$ electrons are already localized, so

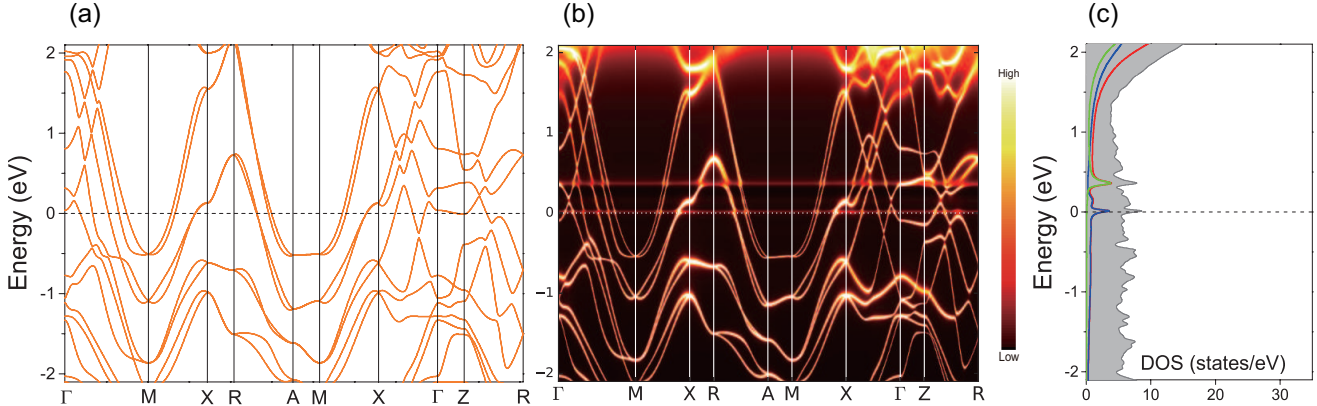


FIG. 9: (a) 4f Open-core DFT bands of CePt₂Ge₂ and (b) the momentum-resolved spectral function at 10 K via DFT+DMFT calculation. (c) Projected DOS by DFT+DMFT simulation at 10 K, in which the dashed horizontal line represents the Fermi level, grey solid line denotes total DOS, red line denotes Ce-4f DOS, blue and green lines show projected Ce-4f_{5/2} and 4f_{7/2} DOS, respectively.

now the Dirac fermions are composed of non-correlated light conduction electrons. Besides, the energy ranges of the DNLs in these two cases are shifted dramatically, in that the energy of the non-interacting DNLs is much far from the Fermi level than the interacting DNLs.

Now we turn to discuss CePt₂Ge₂. By contrast, the transition to Kondo-coherent state upon cooling in CePt₂Si₂ does not emerge in CePt₂Ge₂. In Fig. 9, we compare the 4f open-core DFT bands with the DFT+DMFT momentum-resolved spectral function at 10 K for CePt₂Ge₂, which shows good correspondence. Even at such low temperature, the Ce-4f states just contribute a small DOS near the Fermi level, and the 4f peak height is much smaller than that of CePt₂Si₂ at low temperature. Besides, at 10 K, the imaginary 4f_{5/2} self-energy of CePt₂Ge₂ has very large value at $\omega = 0$, similar to CeSb and γ -Ce which are in local-moment region. Therefore, the 4f electrons are localized, suggesting the local-moment nature of Ce-4f states in CePt₂Ge₂, which can be directly verified by the similarity of 4f open-core DFT bands with the spectral function in Fig. 9. The strong suppression of Ce-4f resonance peak in CePt₂Ge₂ results from about 7% volume increase of the unit cell than CePt₂Si₂, which also drives the itinerant-localized shift of f electrons in CeIn₃ and $\alpha - \gamma$ transition of Ce metal^{19,23}. Since the correlated 4f electrons are localized, the X-R and M-A DNLs in CePt₂Ge₂ are non-interacting, and their energy ranges are (-0.708 eV, -0.615 eV) and (0.129 eV, 0.731 eV) for X-R, (-0.521 eV, -0.507 eV) for M-A, all relatively far from the Fermi level.

V. CONCLUSION AND DISCUSSION

To summarize, we have performed systematic DFT+DMFT simulations of CePt₂Si₂ and CePt₂Ge₂ in a wide temperature

range. By examining the temperature dependence of Ce-4f self-energies, Kondo resonance peak, magnetic susceptibility, and momentum-resolved spectral for CePt₂Si₂, we have verified a crossover from localization of Ce-4f electrons to local Kondo screening of 4f electrons by *spd* conduction electrons, at Kondo screening temperature $T_{KS} \approx 600$ K upon cooling. Secondly, as temperature decreases further, a transition takes place from local Kondo screening to Kondo coherent state in CePt₂Si₂ at coherence temperature $T_{coh} \approx 80$ K, and the Kondo coherence is driven by indirect RKKY interaction between 4f electrons. In contrast, due to larger unit-cell volume than CePt₂Si₂, Ce-4f electrons in CePt₂Ge₂ remain localized as low as 10 K.

The lattice nonsymmorphic symmetries in CePt₂Si₂ and CePt₂Ge₂ give rise to symmetry-protected DNLs along X-R and M-A high-symmetry paths in the Brillouin zone, which are robust under action of SOC and electron correlations. For CePt₂Si₂ above T_{KS} , the local-moment nature of Ce-4f electrons makes these DNLs non-interacting, mainly composing by light *spd* conduction electrons, and the energy windows of these DNLs are relatively far from the Fermi level. Below T_{coh} , the emergence of Kondo coherence drives the DNLs in CePt₂Si₂ strongly interacting and constructing by heavy-fermions with strongly enhanced effective mass and reduced velocity. Remarkably, the energy range of the interacting DNLs is shifted to be much closer to the Fermi level. In intermediate temperature range $T_{coh} < T < T_{KS}$, the DNLs are no longer well identified. By comparison, in CePt₂Ge₂, the DNLs along X-R and M-A paths are non-interacting in wide temperature region, consisting of only light conduction electrons.

It is well known that in some rare-earth semimetallic compounds, Weyl fermions can arise due to breaking of time-reversal symmetry by magnetic order, such as in Weyl node-

point semimetals CeSb^{26,31,32}, CeBi^{33,34}, CeAlGe, CeAlSi and LaAlSi³⁵⁻³⁸; or arise by breaking of space-inversion symmetry in noncentrosymmetric lattices, such as in Weyl node-point semimetal CeRu₄Sn₆³⁹, and Weyl node-ring semimetals Ce₃Bi₄Pt₃^{10,11} and YbCdGe⁴⁰. In addition, Dirac fermions also emerge in node-line Dirac semimetals CeRhSb and CeNiSn with centrosymmetric structures¹⁴. Although model studies have implied that heavy-Weyl or heavy-Dirac quasiparticles can emerge in Anderson lattice model^{41,42}, their appearance in real materials are rare. In most of above materials (except for Weyl semimetals CeRu₄Sn₆ and Ce₃Bi₄Pt₃), the *f* electrons in rare-earth atoms are actually localized, so the Weyl or Dirac fermions in these materials are composed of non-interacting conduction electrons. It should be also stressed that nonsymmorphic CeSbTe also holds DNLs in its paramagnetic phase, however, CeSbTe shows a magnetic order below 2.7 K, and the Ce-4*f* states are essentially localized in its paramagnetic phase⁴³, so their DNLs are formed by conduction electrons in all temperature region. In this context, our revealed interacting DNLs in CePt₂Si₂ provides a very rare case of interacting Dirac fermions in real materials, besides, the dramatic change of Dirac fermions near the DNLs at different temperature regions provides a unique platform for future experimental investigations.

The bulk DNLs and induced surface states have been observed by ARPES experiments in nonsymmorphic ZrSiS⁵⁻⁷ and PtPb₄⁸, which exhibit non-interacting DNLs on the boundaries of their Brillouin zones, likewise, the interacting DNLs we proposed in CePt₂Si₂ also locate along high-symmetric X-R and M-A lines, making it easier to be observed experimentally, and the drastic temperature variation of dis-

persions near the DNLs can also be detected conveniently. We find that the surface states induced by DNLs in CePt₂Si₂ depend sensitively on the cleavage plane of the crystal, hence it requires further experimental data to obtain detailed surface dispersions. Besides, the interacting DNLs below T_{coh} may give rise to heavy surface states which are distinct to ordinary light surface states above T_{KS} ⁴⁴.

According to model studies of Weyl Kondo semimetals, the interacting node point or node line can give rise to unusual transport phenomena in comparison with non-interacting cases, e.g., the strong mass enhancement and velocity reduction of Weyl nodes produce a T^3 temperature dependence of specific heat¹⁰, while the Weyl node line provides two-dimensional Weyl fermions in momentum space, hence contributes a T^2 dependence of specific heat³⁰. Moreover, the electron correlations in topological semimetals can induce nonlinear-response phenomena such as giant spontaneous Hall effect, as observed in node-line Weyl semimetal Ce₃Bi₄Pt₃^{12,13}. Similarly, the interacting DNLs in CePt₂Si₂ may also induced anomalous nonlinear responses, which deserves further experimental and theoretical investigations.

Acknowledgments

This work is supported by GuikeAD20159009, National Natural Science Foundation of China (NO. 12004048, 11864008 and 11764010), the National Key Research and Development Program of China (No. 2021YFB3501503), and the Foundation of LCP.

* Electronic address: lihuan@glut.edu.cn

¹ Zhijun Wang, Yan Sun, Xing-Qiu Chen, Cesare Franchini, Gang Xu, Hongming Weng, Xi Dai, and Zhong Fang, *Phys. Rev. B* **85**, 195320 (2012).
² Zhijun Wang, Hongming Weng, Quansheng Wu, Xi Dai, and Zhong Fang, *Phys. Rev. B* **88**, 125427 (2013).
³ B. Q. Lv, H. M. Weng, B. B. Fu, X. P. Wang, H. Miao, J. Ma, P. Richard, X. C. Huang, L. X. Zhao, G. F. Chen, Z. Fang, X. Dai, T. Qian, and H. Ding, *Phys. Rev. X* **5**, 031013 (2015).
⁴ Zhenwei Wang, Kaifa Luo, Jianzhou Zhao, Rui Yu, , *Phys. Rev. B* **100**, 205117 (2019).
⁵ B.-B. Fu, C.-J. Yi, T.-T. Zhang, M. Caputo, J.-Z. Ma, X. Gao, B. Q. Lv, L.-Y. Kong, Y.-B. Huang, M. Shi, V. N. Strocov, C. Fang, H.-M. Weng, Y.-G. Shi, T. Qian, and H. Ding, *arXiv:1712.00782*.
⁶ Leslie M. Schoop, Mazhar N. Ali, Carola Straßer, Andreas Topp, Andrei Varykhalov, Dmitry Marchenko, Viola Duppel, Stuart S. P. Parkin, Bettina V. Lotsch, and Christian R. Ast, *Nature Communications* **7**, 11696 (2015).
⁷ C. Chen, X. Xu, J. Jiang, S.-C. Wu, Y. P. Qi, L. X. Yang, M. X. Wang, Y. Sun, N. B. M. Schröter, H. F. Yang, L. M. Schoop, Y. Y. Lv, J. Zhou, Y. B. Chen, S. H. Yao, M. H. Lu, Y. F. Chen, C. Felser, B. H. Yan, Z. K. Liu, and Y. L. Chen, *Phys. Rev. B* **95**, 125126 (2017).
⁸ Han Wu, Alannah M. Hallas, Xiaochan Cai, Jianwei Huang, Ji Seop Oh, Vaideesh Loganathan, Ashley Weiland, Gregory T. Mc-

Candless, Julia Y. Chan, Sung-Kwan Mo, Donghui Lu, Makoto Hashimoto, Jonathan Denlinger, Robert J. Birgeneau, Andriy H. Nevidomskyy, Gang Li, Emilia Morosan, and Ming Yi, *npj Quantum Materials* **7**, 31 (2022).
⁹ Steve M. Young, Charles L. Kane, *Phys. Rev. Lett.* **115**, 126803 (2015).
¹⁰ Hsin-Hua Lai, Sarah E. Grefe, Silke Paschen, and Qimiao Si, *Proc. Natl. Acad. Sci. USA* **115**, 93 (2018).
¹¹ Chao Cao, Guo-Xiang Zhi, and Jian-Xin Zhu, *Phys. Rev. Lett.* **124**, 166403 (2020).
¹² Akira Kofuji, Yoshihiro Michishita, and Robert Peters, *Phys. Rev. B* **104**, 085151 (2021).
¹³ S. Dzsaber, X. Yan, M. Taupin, G. Eguchi, A. Prokofiev, T. Shiroka, P. Blaha, O. Rubel, S. E. Grefe, H.-H. Lai, Q. Si, and S. Paschen, *Proc. Natl. Acad. Sci. USA* **118**, e2013386118 (2021).
¹⁴ T.-S. Nam, Chang-Jong Kang, D.-C. Ryu, Junwon Kim, Heejung Kim, Kyoo Kim, and B. I. Min, *Phys. Rev. B* **99**, 125115 (2019).
¹⁵ A. Dommann, F. Hulliger, and H. R. Ott, V. Gramlich, *Journal of the Less-Common Metals* **110**, 331 (1985).
¹⁶ P. Dalmas de Réotier, A. Yaouanc, R. Calemczuk, A. D. Huxley, C. Marcenat, P. Bonville, P. Lejay, P. C. M. Gubbens, and A. M. Mulders, *Phys. Rev. B* **55**, 2737 (1997).
¹⁷ K. Haule, C.-H. Yee, and K. Kim, *Phys. Rev. B* **81**, 195107 (2010).
¹⁸ P. Blaha, K. Schwarz, F. Tran, R. Laskowski, G. K. H. Madsen, and L. D. Marks, *J. Chem. Phys.* **152**, 074101 (2020).

- ¹⁹ Haiyan Lu and Li Huang, *Phys. Rev. B* **94**, 075132 (2016).
- ²⁰ J. H. Shim, K. Haule, and G. Kotliar, *Science* **318**, 1615 (2007).
- ²¹ Xie-Gang Zhu, Yu Liu, Ya-Wen Zhao, Yue-Chao Wang, Yun Zhang, Chao Lu, Yu Duan, Dong-Hua Xie, Wei Feng, Dan Jian, Yong-Huan Wang, Shi-Yong Tan, Qin Liu, Wen Zhang, Yi Liu, Li-Zhu Luo, Xue-Bing Luo, Qiu-Yun Chen, Hai-Feng Song, and Xin-Chun Lai, *npj Quantum Materials* **5**, 47 (2020).
- ²² Yue-Chao Wang, Yuan-Ji Xu, Yu Liu, Xing-Jie Han, Xie-Gang Zhu, Yi-feng Yang, Yan Bi, Hai-Feng Liu, and Hai-Feng Song, *Phys. Rev. B* **103**, 165140 (2021).
- ²³ Q. Y. Chen, W. Feng, D. H. Xie, X. C. Lai, X. G. Zhu, and L. Huang, *Phys. Rev. B* **97**, 155155 (2018).
- ²⁴ C. Ayache, J. Beille, E. Bonjour, R. Calemczuk, G. Creuzet, D. Gignoux, A. Najib, D. Schmitt, J. Voiron, and M. Zerguine, *Journal of Magnetism and Magnetic Materials* **63**, **64**, 329 (1987).
- ²⁵ M.B. Tchoula Tchokonté, P. de V. du Plessis, A.M. Strydom, *Solid State Communications* **136**, 450 (2005).
- ²⁶ Haiyan Lu and Qin Liu, *J. Phys.: Condens. Matter* **32**, 485601 (2020).
- ²⁷ M.B. Tchoula Tchokonté, P. de V. du Plessis, A.M. Strydom, D. Kaczorowski, *Journal of Magnetism and Magnetic Materials* **226**, 173 (2001).
- ²⁸ T.-S. Nam, Junwon Kim, Chang-Jong Kang, Kyoo Kim, and B. I. Min, *Phys. Rev. B* **103**, 045101 (2021).
- ²⁹ S. Burdin, A. Georges, D. R. Grempel, *Phys. Rev. Lett.* **85**, 1048 (2000).
- ³⁰ Lei Chen, Chandan Setty, Haoyu Hu, Maia G. Vergniory, Sarah E. Grefe, Andrey Prokofiev, Silke Paschen, Jennifer Cano, and Qimiao Si, arXiv: 2107.10837.
- ³¹ Chunyu Guo, Chao Cao, Michael Smidman, Fan Wu, Yongjun Zhang, Frank Steglich, Fu-Chun Zhang, and Huiqiu Yuan, *npj Quantum Materials* **2**, 39 (2017).
- ³² Y. Fang, F. Tang, Y. R. Ruan, J. M. Zhang, H. Zhang, H. Gu, W. Y. Zhao, Z. D. Han, W. Tian, B. Qian, X. F. Jiang, X. M. Zhang, and X. Ke, *Phys. Rev. B* **101**, 094424 (2020).
- ³³ Shuchun Huan, Xianbiao Shi, Lixuesong Han, Hao Su, Xia Wang, Zhiqiang Zou, Na Yua, Weiwei Zhao, Leiming Chene, Yanfeng Guo, *Journal of Alloys and Compounds* **875**, 159993 (2021).
- ³⁴ Christian E. Matt, Yu Liu, Harris Pirie, Nathan C. Drucker, Na Hyun Jo, Brinda Kuthanazhi, Zhao Huang, Christopher Lane, Jian-Xin Zhu, Paul C. Canfield, and Jennifer E. Hoffman, *Phys. Rev. B* **105**, 085134 (2022).
- ³⁵ Guoqing Chang, Bahadur Singh, Su-Yang Xu, Guang Bian, Shin-Ming Huang, Chuang-Han Hsu, Ilya Belopolski, Nasser Ali-doust, Daniel S. Sanchez, Hao Zheng, Hong Lu, Xiao Zhang, Yi Bian, Tay-Rong Chang, Horng-Tay Jeng, Arun Bansil, Han Hsu, Shuang Jia, Titus Neupert, Hsin Lin, and M. Zahid Hasan, *Phys. Rev. B* **97**, 041104(R) (2018).
- ³⁶ Pascal Puphal, Vladimir Pomjakushin, Naoya Kanazawa, Victor Ukleev, Dariusz J. Gawryluk, Junzhang Ma, Muntaser Naamneh, Nicholas C. Plumb, Lukas Keller, Robert Cubitt, Ekaterina Pom-jakushina, and Jonathan S. White, *Phys. Rev. Lett.* **124**, 017202 (2020).
- ³⁷ Hao Su, Xianbiao Shi, Jian Yuan, Yimin Wan, Erjian Cheng, Chuanying Xi, Li Pi, Xia Wang, Zhiqiang Zou, Na Yu, Weiwei Zhao, Shiyuan Li, and Yanfeng Guo, *Phys. Rev. B* **103**, 165128 (2021).
- ³⁸ Anup Pradhan Sakhya, Cheng-Yi Huang, Gyanendra Dhakal, Xue-Jian Gao, Sabin Regmi, Xiaohan Yao, Robert Smith, Milo Sprague, Bahadur Singh, Hsin Lin, Su-Yang Xu, Fazel Tafti, Arun Bansil, and Madhab Neupane, arXiv:2203.05440.
- ³⁹ Yuanfeng Xu, Changming Yue, Hongming Weng, and Xi Dai, *Phys. Rev. X* **7**, 011027 (2017).
- ⁴⁰ Antu Laha, Sudip Malick, Ratnadwip Singha, Prabhat Mandal, P. Rambabu, V. Kanchana, and Z. Hossain, *Phys. Rev. B* **99**, 241102(R) (2019).
- ⁴¹ Sarah E. Grefe, Hsin-Hua Lai, Silke Paschen, and Qimiao Si, *Phys. Rev. B* **101**, 075138 (2020).
- ⁴² Po-Yao Chang and Piers Coleman, *Phys. Rev. B* **97**, 155134 (2018).
- ⁴³ Leslie M. Schoop, Andreas Topp, Judith Lippmann, Fabio Orlandi, Lukas Müchler, Maia G. Vergniory, Yan Sun, Andreas W. Rost, Viola Duppel, Maxim Krivenkov, Shweta Sheoran, Pascal Manuel, Andrei Varykhalov, Binghai Yan, Reinhard K. Kremer, Christian R. Ast, and Bettina V. Lotsch, *Sci. Adv.* **4**, 2317 (2018).
- ⁴⁴ Robert Peters, Tsuneya Yoshida, Hirofumi Sakakibara, and Norio Kawakami, *Phys. Rev. B* **93**, 235159 (2016).